Defect evolution in ultralow energy, high dose helium implants of silicon performed at elevated temperatures

K. Haynes (iD), X. Hu, B. D. Wirth, C. Hatem, and K. S. Jones

View Online   Export Citation   CrossMark

ARTICLES YOU MAY BE INTERESTED IN

CrossMark
click for updates

Defect evolution in ultralow energy, high dose helium implants of silicon performed at elevated temperatures

K. Haynes,[1,a] X. Hu,[2] B. D. Wirth,[2,3] C. Hatem,[4] and K. S. Jones[1]
[1]*Department of Materials Science and Engineering, University of Florida, Gainesville, Florida 32611, USA*
[2]*Oak Ridge National Laboratory, Oak Ridge, Tennessee 37831, USA*
[3]*Department of Nuclear Engineering, University of Tennessee, Knoxville, Tennessee 37996, USA*
[4]*Applied Materials, Gloucester, Massachusetts 01930, USA*

There is a growing interest in using high dose helium implants to alter point defect populations in silicon. Previous reports have shown that the interaction between helium and vacancies leads to the formation of cavities for medium energy (e.g., 20–100 keV) implants. However, the role of certain factors, such as the proximity of the surface, the damage created by the implant, and the effect of the implant temperature, is not well understood for low energy implants. This study explored a new regime of ultralow energy, elevated temperature implants in order to offer an insight into the effect of these parameters. Transmission electron microscopy (TEM) showed that cavity formation was avoided for 0.5 keV, 450 °C implants up to a dose of 8×10^{16} cm^{-2}. However, extended defects in the form of {311} ribbon-like defects and stacking faults were observed. Quantitative TEM showed that the number of interstitials in these defects was less than 0.2% of the implant dose. In addition, thermal helium desorption spectrometry suggested that only 2% of the implanted He dose was retained in interstitial He and He$_m$V$_n$ complexes. A first-order dissociation kinetic model was applied to assess desorption from He$_m$V$_n$, which closely matched energies predicted by density functional theory. This population of excess vacancies and excess interstitials was possibly formed because of incomplete Frenkel pair recombination. Raman spectroscopy showed that the stress from the implant was dominated by the stress from the interstitial-type defects. The evolution of the stress and defects was also explored as a function of post-implant annealing. *Published by AIP Publishing.* https://doi.org/10.1063/1.5046096

I. INTRODUCTION

High-dose, medium-energy He implants in Si are known to result in the formation of He bubbles.[1] Upon high temperature annealing, these bubbles outgas He and grow into larger cavities via either migration and coalescence[2,3] or an Ostwald-ripening process.[4,5] Many studies have explored the morphology and evolution of these cavities,[5] which have applications for ion-cut technology,[6] gettering transition metal impurities,[7,8] gettering dopants,[9–11] and reducing interstitial populations.[12,13]

Cavity formation is believed to occur because of the interaction between He and vacancies. Due to its low solubility in Si, He is energetically driven to occupy sites with the largest available free volume. When He is introduced into Si by ion implantation, elastic collisions generate a large number of vacancies and self-interstitials. These point defects are mobile even at room temperature in Si and will either recombine with one another or form larger defect clusters. Helium will preferentially occupy vacancy clusters, and multiple He atoms can be accommodated within these vacancy clusters,[14] leading to the formation of He$_m$V$_n$ complexes of varying sizes. These clusters are precursors to larger He bubbles.

He$_m$V$_n$ clusters could be used as a source of vacancies for improving dopant activation. Modern devices may require dopant activation levels in excess of their solid solubilities in Si, and it is often not possible to use dopant activation methods such as melting or solid-phase epitaxial regrowth with 3D device architectures.[15] Vacancy engineering approaches are needed, and He may be able to disrupt self-interstitial-vacancy recombination in favor of excess vacancies.

Because of the strong interaction of He with the point defects generated by the implantation process, changes to the implant conditions can have a dramatic effect on the defect structures that are generated. Elevated temperature He implants have been shown to result in different defect structures compared to room temperature implants.[16–20] A lower density of larger He bubbles is formed at moderate implant temperatures (e.g., 200–600 °C), while bubble formation is entirely suppressed at higher implant temperatures.[19] Extended defects have also been observed in the form of {311} rod- and ribbon-like defects and dislocation loops.[19] This range of defects reflects the complex kinetics of the atomic processes involved, which include self-interstitial-vacancy recombination, point defect diffusion, and He diffusion, as well as the relative stabilities of various defect complexes at different temperatures.

Previous studies of elevated temperature He implants were completed for implant energies greater than 20 keV. This results in projected ranges in excess of 200 nm due to the light mass of He. There have been few studies on low energy implantation of He into Si.[21,22] The proximity of the surface is expected to play a role in He implantation

---

a)Author to whom correspondence should be addressed: kschuller@ufl.edu

dynamics, as it can act as a sink for either self-interstitials or vacancies, as well as He desorption. In addition, lower energy implants generate fewer Frenkel pairs per ion, which is likely to impact their interaction with He.

In this study, the defect evolution of ultralow energy, elevated temperature He implants is investigated. Cavity formation and other defect structures are found to vary widely from their corresponding higher energy implants. The dynamics of He and point defect interactions is explored, which offers some insight into the evolution of Frenkel pairs in the absence of excess interstitials that are typically generated by implanting dopant species.

II. EXPERIMENT

He$^+$ was implanted into *n*-type Czochralski-grown (100) Si at 450 °C using an implantation energy of 0.5 keV. Doses were varied from 5×10^{15} to 8×10^{16} cm^{-2} and beam currents of approximately 4 mA were used. Both rapid thermal anneals (RTA) and furnace anneals were investigated for temperatures between 500 °C and 1000 °C under an Ar ambient.

Damage evolution was monitored by cross-section and plan-view transmission electron microscopy (TEM). Cross-sections were prepared with a focused ion beam using standard methods. Self-supported plan-view samples were prepared by coring 3-mm discs, which were then polished and etched from the backside to obtain regions of electron transparency. TEM characterization was performed on an FEI Tecnai F20 microscope using [110] zone axis imaging conditions for the cross-sections and $\mathbf{g}_{220}$ weak beam dark field (WBDF) imaging conditions for the plan-view samples.

Raman spectroscopy was used to determine stress in the implanted region. Spectra were collected on an Horiba Aramis microRaman system with an excitation wavelength of 325 nm. This wavelength has a penetration depth of approximately 10 nm, which closely matches the depth of the implants investigated.

Thermal helium desorption spectrometry (THDS) was used to measure the desorption of He as a function of temperature for a constant ramp rate of 0.5 °C/s up to 1250 °C. Released He was measured by a quadrupole mass spectrometer. The ultra-high vacuum chamber ($\sim 1 \times 10^{-9}$ Torr) provides a low He background of 2×10^{10} He/s. Measurements were calibrated with a high-precision glass-permeation helium calibrated leak.

III. RESULTS AND DISCUSSION

Depth distributions for He and for Frenkel pairs generated by the implant were calculated using SRIM-2013, a Monte Carlo simulation program.[23] Results are shown for the 2×10^{16} cm^{-2} dose in Fig. 1. The projected range for He is 8.6 nm with the peak concentration located at 6.8 nm, while the peak of the vacancy distribution is at a depth of 3.6 nm. On average, each He ion generates 8 Frenkel pairs, according to SRIM. However, SRIM does not account for thermal effects, such as diffusion or recombination of implanted species or point defects. Thus, this simulation is an estimate of the distribution of Frenkel pairs generated during the implant. It is expected that most of these Frenkel pair defects
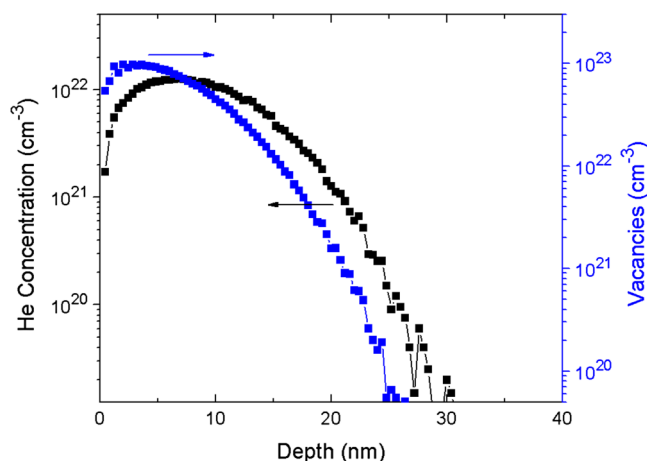

FIG. 1. SRIM simulations for the He distribution and vacancy distribution for a 2×10^{16} He/cm^2 implant at 0.5 keV.

will either recombine at the 450 °C implant temperature or annihilate at the free surface, leaving only a small fraction of the initial point defect population behind. Likewise, some fraction of the interstitial helium will likely diffuse back to the surface and desorb.

He bubble formation in Si has been found to be primarily dependent on the local He concentration for room temperature implants. When concentrations exceed $3 \ (\pm 1) \times 10^{20}$ cm^{-3}, bubbles have been observed.[7] Based on the peak concentrations of He for the doses in this study, all samples would be expected to form He bubbles if 100% of the implanted helium were retained. However, some fraction is likely to diffuse out at the high implant temperature. It should also be noted that a significant portion (21%) of the incident ions are reflected (backscattered) from the sample without implanting. In addition, sputtering effects are non-negligible for the two highest doses. SRIM estimates that approximately 3.1 and 1.6 nm are sputtered from the surface for a dose of 8×10^{16} and 4×10^{16} cm^{-2}, respectively. Using an iterative method to account for the moving surface during implantation,[24] the amount of He lost due to sputtering is estimated to be less than 6% and 3%, respectively. Adjusted ion and vacancy profiles for the highest dose are provided in the supplementary material.

TEM cross-sections were prepared for each of the implanted doses, as shown in the high-resolution TEM (HRTEM) images in Fig. 2. No He bubbles were visible, even for the highest doses. However, extended defects were visible for doses above 5×10^{15} cm^{-2}. Stacking faults along {111} planes and ribbon-like {311} defects were both observed (Fig. 3). The defect density appeared to increase proportionally with the dose. The defects were largely present within 30 nm of the surface, corresponding to the damage profile predicted by SRIM. However, some of the defects were located considerably deeper, up to 60 nm beneath the surface. This indicates that the point defects that make up the extended defects were very mobile at the implant temperature and may have nucleated heterogeneously on an impurity or pre-existing defect.

Fast Fourier Transform (FFT) filtering was used to investigate the nature of the extended defects. Implant damage is typically interstitial in nature, as explained by the "plus-one" model.[25] Most interstitial-vacancy pairs recombine during
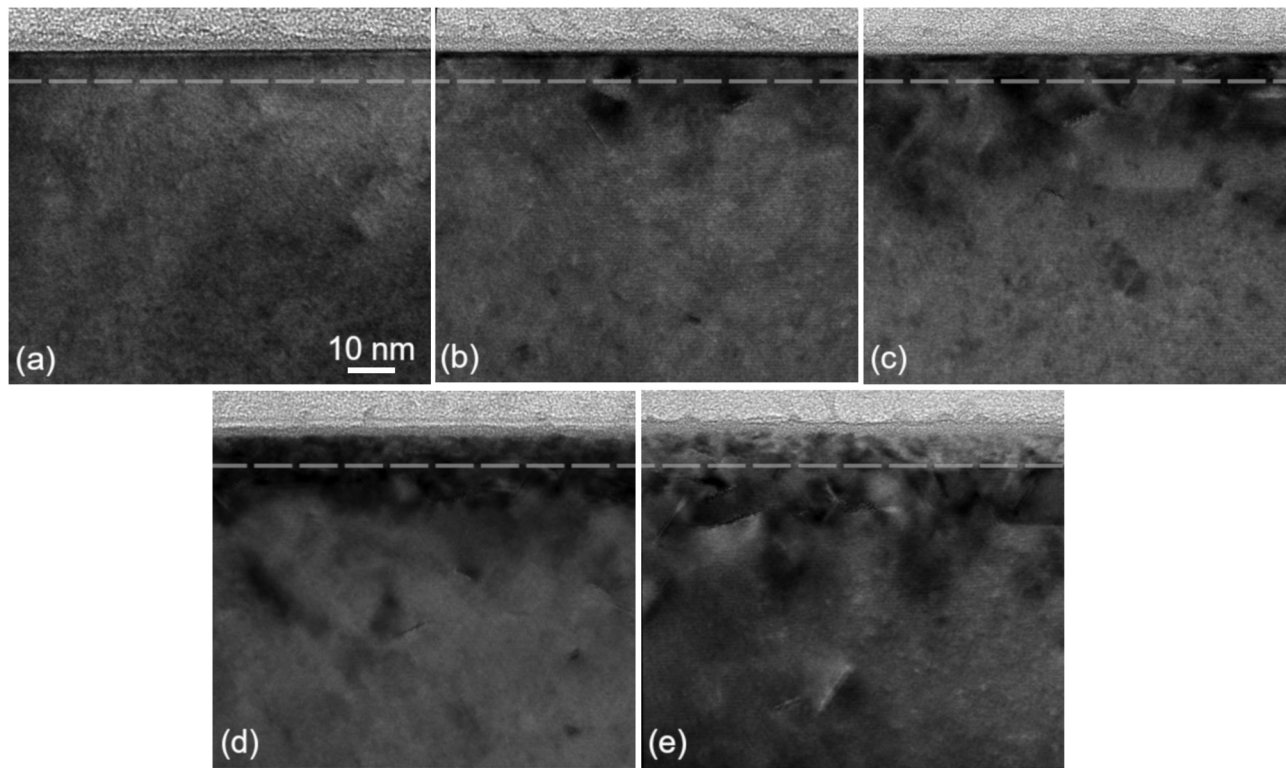
FIG. 2. Cross-sectional HRTEM images of Si implanted at 0.5 keV and 450 °C with (a) 5×10^{15}, (b) 1×10^{16}, (c) 2×10^{16}, (d) 4×10^{16}, and (e) 8×10^{16} He/cm^2. The projected range of the He is indicated by a dashed line.

implantation and upon annealing, leaving behind a quantity of interstitials that is approximately equal to the implanted dose. However, He is dynamically removed during elevated temperature implant, and the dominant observable defects after He implantation are generally cavities, i.e., large vacancy clusters that may contain He. Therefore, the nature of these extended defects needs to be carefully examined to determine whether it is intrinsic or extrinsic. A representative HRTEM image of a stacking fault and an FFT filtered image are shown in Fig. 4. The lattice fringes clearly bow outward around the stacking fault, indicating that it is made up of an inserted plane of atoms and confirming its extrinsic nature.
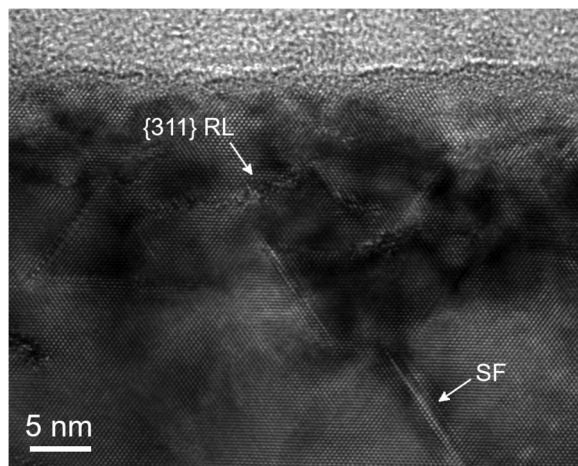
The fact that cavities were not formed is a departure from higher energy studies that were completed at similar implant temperatures and doses. David and Oliviero observed cavity formation for 50 keV 5×10^{16} He/cm^2 implants completed at implant temperatures up to 600 °C.[18,19,26,27] Bubble formation did not occur in this study. This may indicate that the proximity of the surface allows He to escape more efficiently than for a higher energy implant. It could also be related to the lower number of vacancies generated. According to SRIM calculations, a 0.5 keV implant creates about 8 vacancies/ion compared to ~166 vacancies/ion for a 50 keV implant. Despite this difference in He bubble formation, the interstitial-type defects observed are similar to the higher-energy implantation studies, which also noted rod-like defects, ribbon-like defects, and dislocation loops for temperatures above 600 °C. Babonneau also observed {311} rod- and ribbon-like defects following 50 keV

FIG. 3. Extended defects for an 8×10^{16} He/cm^2 implant at 0.5 keV and 450 °C included both stacking faults (SF) along {111} planes and {311} ribbon-like (RL) defects.
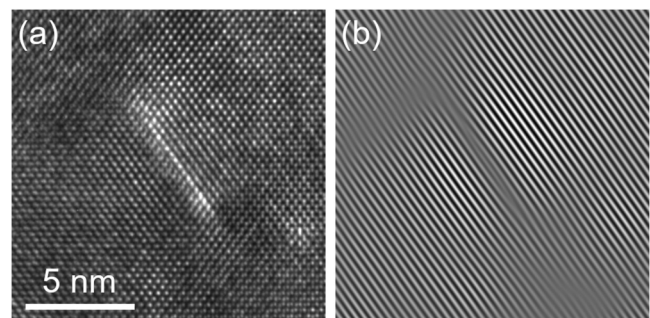

FIG. 4. (a) HRTEM image of a stacking fault following a 0.5 keV, 450 °C implant. (b) An FFT filtered image shows the lattice fringes bowing around the stacking fault, indicating its extrinsic nature.

helium implantation to a dose of 7×10^{15} He/cm^2 at implant temperatures above 300 °C.[20]

THDS revealed two desorption peaks, as shown in the results for the 8×10^{16} cm^{-2} dose of Fig. 5. A higher intensity peak was centered at ~65 °C, while a lower intensity peak was centered at ~300 °C. Both desorption peaks have been previously observed and have been attributed to interstitial He[22,28] and He$_m$V$_n$ traps,[1,22,29] respectively. There was no desorption peak between 700 °C and 1200 °C as would be expected if there were He bubbles present. The total retained He dose (as determined from the integrated THDS signal) was determined to be 1.3×10^{15} cm^{-2} for the 8×10^{16} cm^{-2} dose. This represents approximately 2% of the implanted He dose. The total retained He is observed to increase with increasing implantation dose. For example, retained doses of 1.8% and 1.2% were calculated for the 4×10^{16} and 2×10^{16} cm^{-2} doses, respectively. Values for the lower dose samples were not determined, as the detection sensitivity of the THDS was reached at lower implanted helium contents.

For the highest dose of 8×10^{16} cm^{-2}, approximately 80% of the retained He is associated with the lower temperature desorption peak, while the remaining 20% is associated with the higher temperature desorption peak. For the lower dose samples, a larger fraction of the retained dose is associated with the higher temperature peak. For example, the 2×10^{16} cm^{-2} dose has approximately 60% retained He in the lower temperature desorption peak and 40% in the higher temperature desorption peak.

The retained doses are much lower than have been observed for higher energy He implants at similar implant temperatures. For example, Oliviero observed 65% and 25% helium retention for 400 °C and 500 °C implants at 50 keV, respectively.[18] At higher implantation energies (and temperatures), helium was retained in cavities, which have a characteristic desorption temperature between 700 and 1200 °C. This means that the retained helium could only desorb at

FIG. 5. THDS for an 8×10^{16} He/cm^2 implant at 0.5 keV and 450 °C. A constant ramp rate of 0.5 °C/s was used. The line is a calculation for the expected desorption based on a first-order kinetic model with a distribution of activation energies. (Inset) The low temperature desorption peak for the same sample.

temperatures higher than the implantation temperature. In the case of the ultralow energy implants in this study, He is observed to predominantly desorb below the implantation temperature of 450 °C. The traps that are associated with these low temperature peaks are not effective in trapping He at the implant temperature. This implies that, after the sample has cooled to room temperature following the implant, only the residual He that has been unable to diffuse out of the Si has been retained. Evidently, there is something unique about the low energy implant that prevents He$_m$V$_n$ clusters from reaching the critical size necessary to form larger cavities. Again, it is likely this is related to the proximity of the surface or the lower number of vacancies generated compared to a higher energy implant.

Desorption of He from Si is often modeled as a first-order kinetic reaction. By fitting the THDS data with such a model, the activation energies associated with the two distinct desorption processes can be estimated. The rate of desorption is given by

$$\frac{dN}{dt} = -N\nu \exp\left(-\frac{E}{kT}\right), \qquad (1)$$

where N is the number of He atoms remaining in the sample, ν is the attempt frequency, E is the activation energy, k is the Boltzmann constant, and T is the temperature. Extracting a value for the activation energy requires knowledge of the attempt frequency. The attempt frequency for He desorbing from Si has been observed to be much lower than the expected Debye frequency $(1 \times 10^{13}$ s^{-1}).[1,29] Corni *et al.* calculated that it lies in the range of 3.3×10^7–1.7×10^9 s^{-1}. This range was used in subsequent calculations in this work.

It was found that the high temperature peak (around 300 °C) is not well fit by a single activation energy. As shown by Corni *et al.*, it is more accurately modeled by a distribution of activation energies.[29] This fact reflects that there is a range of energies required to dissociate from various sizes of He$_m$V$_n$ clusters. Using binding energies determined from density function theory,[14] it can be shown that the activation energy distribution might be modeled as a normal distribution (see supplementary material). A best-fit desorption profile calculated from this model is overlaid on the measured desorption data in Fig. 5. The mean of the distribution of activation energies was found to lie in the range of 1.10–1.28 eV, depending on the choice of the attempt frequency, while the standard deviation was 0.17–0.20 eV. These values align quite well with those predicted for He$_m$V$_n$ by density functional theory, which result in a mean of 1.06 eV and a standard deviation of 0.17.[14]

The activation energy for the low temperature peak was determined to lie between 0.59 and 0.69 eV, which also corresponds remarkably well with the activation energy determined by Pizzagalli for interstitial migration of He (0.68 eV).[30] This desorption peak has only been previously observed for low energy helium implants.[21,22] An explanation can be proposed for this unique occurrence. The He remaining at the end of the implant is "frozen" into the nearest low-energy positions, which includes a significant portion on interstitial sites. Upon heating during THDS measurement, the interstitial He will
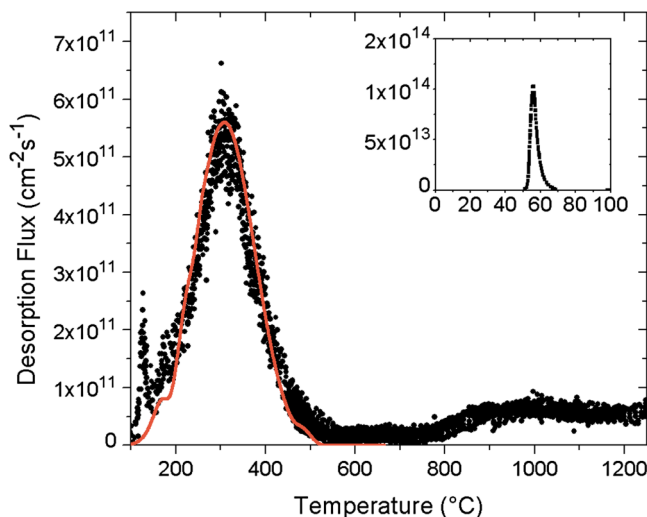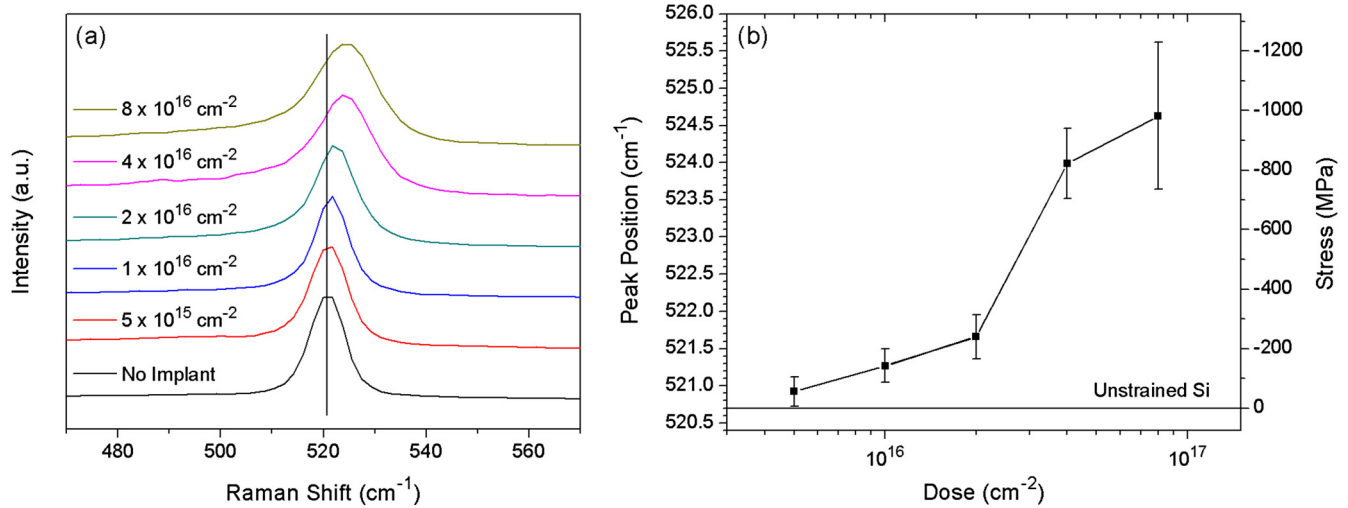
FIG. 6. (a) Raman spectra for the as-implanted samples show increasing blue shifts with increasing He dose. (b) Compressive stresses were calculated from the magnitude of the peak shift. Error bars are 95% confidence intervals based on multiple measurements across a single sample.

diffuse along tetrahedral-hexagonal sites, and some He will reach the surface without becoming trapped. This process is very unlikely for higher energy implants, in which interstitial He is likely to become trapped by the high density of vacancies, He_mV_n clusters, or He bubbles that lie between the projected range of He and the Si surface. This theory is supported by the literature. Corni *et al.* observed a delay time for isothermal desorption of He, which could only be explained by interstitial He trapping and detrapping from vacancy-like defects.[31] This supports the idea that interstitial He is present for higher energy implants as well, but it is unlikely to reach the surface without becoming trapped.

Stress evolution as a function of increasing He dose was studied using Raman spectroscopy. Raman spectroscopy has previously been used to quantify stress in H- and He-implanted Si.[32,33] In these earlier works, the resulting stress was tied to the size and morphology of the spherical nanobubbles or platelets that are formed. No such bubbles were formed by the implants in this study. In addition, much

of the initial He dose has diffused out of the material. Therefore, by elimination, any stress must be closely associated with the extended defects and defect clusters created by the implant.

The primary Raman-active peak for Si is a three-fold degenerate longitudinal optical (LO) mode at $520.7 \, cm^{-1}$. Under stress, this peak splits and a peak shift is induced. Assuming a biaxial stress state, the magnitude of the in-plane stress σ is linearly related to the magnitude of the frequency shift $\Delta\omega$ by

$$\sigma \, (\text{MPa}) = -250 \cdot \Delta\omega \, (cm^{-1}), \tag{2}$$

as has been derived elsewhere.[34] From this equation, it can be seen that a compressive stress will induce an increase in the Raman frequency while a tensile stress will induce a decrease. Using a fitting procedure, the peak position can be determined within approximately $0.1 \, cm^{-1}$, allowing the detection of stresses as low as 25 MPa.
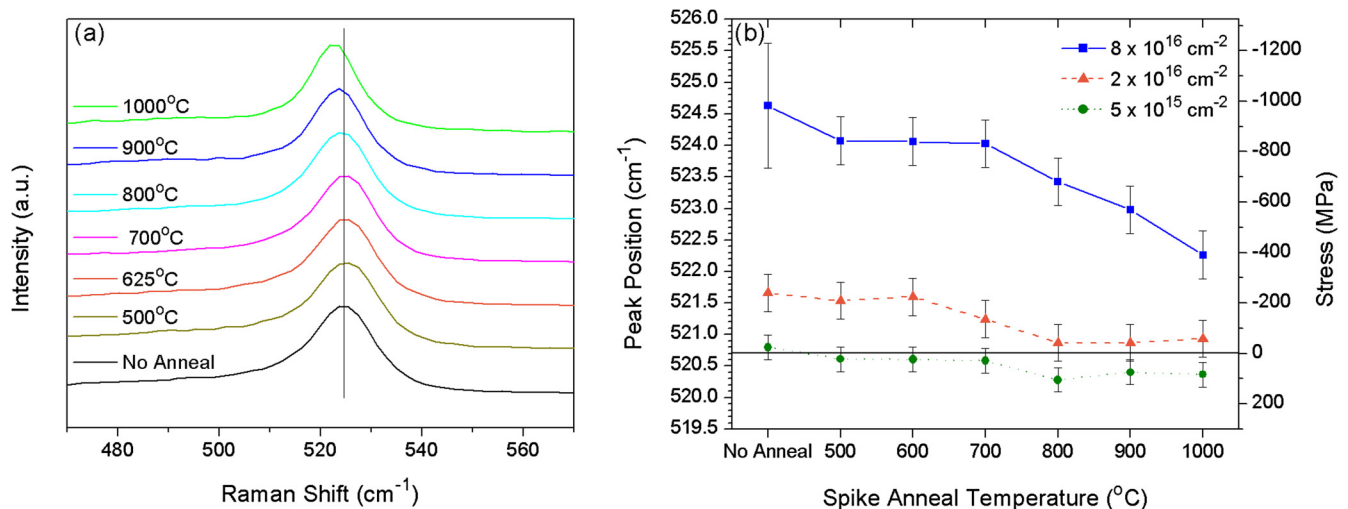

FIG. 7. (a) Raman spectra for the $8 \times 10^{16} \, cm^{-2}$ implant following RTA spike anneals at temperatures from 500 to 1000 °C. (b) Stresses calculated from the magnitude of the peak shifts following annealing for three of the implant doses.
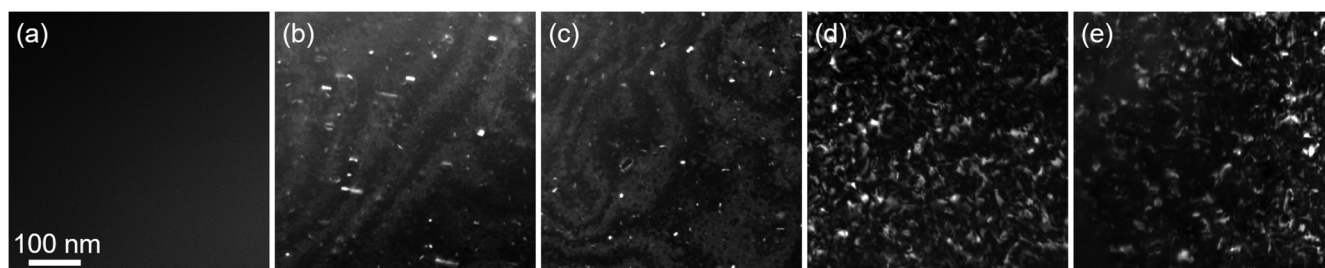
FIG. 8. WBDF TEM images of Si implanted with (a) 5×10^{15}, (b) 1×10^{16}, (c) 2×10^{16}, (d) 4×10^{16}, and (e) 8×10^{16} He/cm^2 at 0.5 keV and 450 °C, following an anneal at 750 °C for 15 min.

Raman spectra for the as-implanted samples are shown in Fig. 6. A Gaussian-Lorentzian fitting procedure was used to determine the peak position. The LO peak shifted to higher Raman frequencies with He implantation. The stress increased monotonically with increasing dose, up to a maximum value of 1 GPa for the 8×10^{16} cm^{-2} dose. The full-width at half-maximum of the peaks also increased with He dose, which can be attributed to the lattice disorder created by the implant.

Generally, self-interstitial defect clusters are expected to induce compressive stresses, while vacancy defect clusters should induce tensile stresses. Given the different configurations taken by interstitial and vacancy clusters as well as the variety of cluster sizes that are likely to be present, it is not possible to deduce the relative concentrations of interstitials and vacancies from these stress measurements. However, it appears that the compressive stresses induced by the interstitial-type defects dominate the overall stress of the system.

Stress was also monitored as a function of annealing temperature for spike anneals performed between 500 °C and 1000 °C. The Raman spectra for the 8×10^{16} cm^{-2} dose are shown in Fig. 7. For this dose, the Raman peak position remained relatively constant around 524.0 cm^{-1} until the 800 °C anneal. At this point, the peak shifted back toward the unstrained peak position but never fully reached the unstressed state. This is roughly the temperature at which self-interstitial-type defects are known to evolve following implantation,[35] which supports the theory that the stress state is closely tied to the defect clusters. Furthermore, as shown by the THDS results of Fig. 6, the majority of the retained He has desorbed by 800 °C. A similar shift in peak position was noted for the lower dose samples but with smaller magnitude shifts toward the unstressed state.

Samples were also annealed for longer times at 750 °C and 900 °C in a furnace in order to observe the evolution of the extended defects. WBDF images obtained using the $\mathbf{g}_{220}$ condition are shown in Fig. 8. After a 15 min anneal at 750 °C, the defects appeared to be primarily category I loops that evolved from the flux of interstitials from dissolved {311}-type defects.[36] There were no loops visible in the 5×10^{15} cm^{-2} sample. Quantitative analysis of multiple anneal times suggested that the as-implanted interstitial population was less than 0.2% of the generated interstitial population across the dose series and that the interstitial population increased in proportion with the dose. After a separate 20 min 900 °C anneal (not shown), the dislocation loops had coarsened and decreased in density.

IV. CONCLUSIONS

High dose (5×10^{15}–8×10^{16} cm^{-2}), ultralow energy (0.5 keV) implants of He into Si were performed at 450 °C. The nature of the low energy implants was found to be different from higher energy implants performed at similar temperatures. No cavities were formed, and approximately 98% of the helium was shown to have desorbed during the implant. THDS analysis revealed that the retained He was likely present as interstitial impurities (60%–80%) and in He$_m$V$_n$ complexes (20%–40%). A first-order dissociation kinetic model fit to the THDS data indicated that the activation energies associated with desorption from the He$_m$V$_n$ complexes closely matched energies predicted by density functional theory. TEM analysis also revealed {311} ribbon-like defects as well as stacking faults. These extended defects evolved into dislocation loops with further annealing. Stress analysis with Raman spectroscopy confirmed that the interstitial-type defects dominated the stress state of the implanted region, even after annealing. These results suggest that the proximity of the surface or the number of Frenkel pairs generated by the implants may play an important role in the defect evolution, changing the dynamics of the interaction between He and point defects.

SUPPLEMENTARY MATERIAL

See supplementary material for a more complete description of the distribution of activation energies as well as the effect of sputtering on the highest dose implant.

ACKNOWLEDGMENTS

[1]C. C. Griffioen, J. H. Evans, P. C. De Jong, and A. Van Veen, Nucl. Instr. Meth. Phys. Res. B **27**, 417 (1987).

[2]J. Evans, Nucl. Instr. Meth. Phys. Res. B **196**, 125 (2002).

[3]M. Hasanuzzaman, Y. M. Haddara, and A. P. Knights, J. Appl. Phys. **112**, 064302 (2012).

[4]S. Frabboni, F. Corni, C. Nobili, R. Tonini, and G. Ottaviani, Phys. Rev. B **69**, 165209 (2004).

[5]V. Raineri, M. Saggio, and E. Rimini, J. Mater. Res. **15**, 1449 (2000).

[6]M. Bruel, Electron. Lett. **31**, 1201 (1995).

[7]V. Raineri, P. G. Fallica, G. Percolla, A. Battaglia, M. Barbagallo, and S. U. Campisano, J. Appl. Phys. **78**, 3727 (1995).

[8]F. Roqueta, L. Ventura, J. J. Grob, and R. Jérisian, J. Appl. Phys. **88**, 5000 (2000).

[9]F. Cayrel, D. Alquier, L. Ventura, and F. Roqueta, Eur. Phys. J. Appl. Phys. **23**, 41 (2003).

[10]F. Roqueta, D. Alquier, L. Ventura, C. Dubois, and R. Jérisian, Nucl. Instr. Meth. Phys. Res. B **183**, 318 (2001).

[11]F. Cayrel, D. Alquier, D. Mathiot, L. Ventura, L. Vincent, G. Gaudin, and R. Jerisian, Nucl. Instr. Meth. Phys. Res. B **216**, 291 (2004).

[12]V. Raineri and S. U. Campisano, Appl. Phys. Lett. **69**, 1783 (1996).

[13]M. L. David, M. F. Beaufort, and J. F. Barbot, Nucl. Instr. Meth. Phys. Res. B **226**, 531 (2004).

[14]L. Pizzagalli, M.-L. David, and J. Dérès, Phys. Status Solidi **214**, 1700263 (2017).

[15]R. Duffy, M. J. H. Van Dal, B. J. Pawlak, M. Kaiser, R. G. R. Weemaes, B. Degroote, E. Kunnen, and E. Altamirano, Appl. Phys. Lett. **90**, 241912 (2007).

[16]V. Raineri and M. Saggio, Appl. Phys. Lett. **71**, 1673 (1997).

[17]P. F. Fichtner, A. Peeva, M. Behar, G. d. M. Azevedo, R. Maltez, R. Koegler, and W. Skorupa, Nucl. Instr. Meth. Phys. Res. B **161–163**, 1038 (2000).

[18]E. Oliviero, M. L. David, M. F. Beaufort, J. F. Barbot, and A. van Veen, Appl. Phys. Lett. **81**, 4201 (2002).

[19]M. L. David, M. F. Beaufort, and J. F. Barbot, J. Appl. Phys. **93**, 1438 (2003).

[20]D. Babonneau, M.-F. Beaufort, A. Declémy, J.-F. Barbot, and J.-P. Simon, J. Appl. Phys. **99**, 113507 (2006).

[21]A. L. M. Davies and G. Carter, Radiat. Eff. **10**, 227 (1971).

[22]A. Van Veen, H. Schut, R. A. Hakvoort, A. Fedorov, and K. T. Westerduin, MRS Proc. **373**, 499 (1994).

[23]J. F. Ziegler, M. D. Ziegler, and J. P. Biersack, Nucl. Instr. Meth. Phys. Res. B **268**, 1818 (2010).

[24]J. Wang, M. B. Toloczko, N. Bailey, F. A. Garner, J. Gigax, and L. Shao, Nucl. Instr. Meth. Phys. Res. B **387**, 20 (2016).

[25]M. D. Giles, J. Electrochem. Soc. **138**, 1160 (1991).

[26]E. Oliviero, M. L. David, A. V. Fedorov, A. van Veen, M. F. Beaufort, and J. F. Barbot, Mater. Sci. Eng. B **102**, 222 (2003).

[27]M. David, A. Ratchenkova, E. Oliviero, M. Denanot, M. Beaufort, A. Declémy, C. Blanchard, N. Gerasimenko, and J. Barbot, Nucl. Instr. Meth. Phys. Res. B **198**, 83 (2002).

[28]A. Van Veen, P. C. De Jong, K. R. Bijkerk, H. A. Filius, and J. H. Evans, MRS Proc. **100**, 231 (1988).

[29]F. Corni, C. Nobili, G. Ottaviani, R. Tonini, G. Calzolari, G. F. Cerofolini, and G. Queirolo, Phys. Rev. B **56**, 7331 (1997).

[30]L. Pizzagalli and A. Charaf-Eddin, Semicond. Sci. Technol. **30**, 085022 (2015).

[31]F. Corni, G. Calzolari, S. Frabboni, C. Nobili, G. Ottaviani, R. Tonini, G. F. Cerofolini, D. Leone, M. Servidori, R. S. Brusa, G. P. Karwasz, N. Tiengo, and A. Zecca, J. Appl. Phys. **85**, 1401 (1999).

[32]C. Villeneuve, V. Paillard, K. K. Bourdelle, I. Cayrefourcq, A. Boussagol, and M. Kennard, Nucl. Instr. Meth. Phys. Res. B **253**, 182 (2006).

[33]C. Villeneuve, K. K. Bourdelle, V. Paillard, X. Hebras, and M. Kennard, J. Appl. Phys. **102**, 094905 (2007).

[34]I. De Wolf, Semicond. Sci. Technol. **11**, 139 (1996).

[35]K. S. Jones, S. Prussin, and E. R. Weber, Appl. Phys. A Solids Surf. **45**, 1 (1988).

[36]J. Li and K. S. Jones, Appl. Phys. Lett. **73**, 3748 (1998).